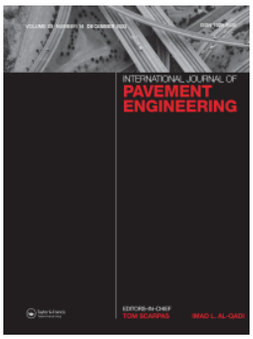

International Journal of Pavement Engineering

ISSN: (Print) (Online) Journal homepage: www.tandfonline.com/journals/gpav20

Tracking particle displacements in unbound aggregate layers of roadways

S. Subramanian & Jorge G. Zornberg

To cite this article: S. Subramanian & Jorge G. Zornberg (2024) Tracking particle displacements in unbound aggregate layers of roadways, International Journal of Pavement Engineering, 25:1, 2345786, DOI: 10.1080/10298436.2024.2345786

To link to this article: https://doi.org/10.1080/10298436.2024.2345786

INTERNATIONAL JOURNAL OF PAVEMENT ENGINEERING
2024, VOL. 25, NO. 1, 2345786
https://doi.org/10.1080/10298436.2024.2345786

Tracking particle displacements in unbound aggregate layers of roadways

S. Subramanian and Jorge G. Zornberg

Civil Engineering, University of Texas, Austin, TX, USA

ABSTRACT

Accelerated pavement tests were conducted on reduced-scale pavement sections under controlled environmental conditions using the model Mobile Load Simulator (MLS11). A unique monitoring system was developed as part of this study to evaluate the response of the pavement sections under rolling wheel loads. The performance of the sections with an increasing number of wheel passes was evaluated by measuring the surface rutting as well as the subsurface displacement of particles within the base layer. The sections were built in modular frames constructed above grade to facilitate access to the particles within the base layer from the sides of the frame. Surface rutting was measured intermittently using an in-house developed laser profilometer. A unique, cost-effective assembly of 30 linear position transducers was designed to continuously track the displacements of artificial particles within the base layer. The displacements, measured with the new system, were found to be particularly suitable to generate horizontal permanent displacement fields and strain fields. Overall, the new developments allowed comprehensive monitoring of the internal response of pavements subjected to wheel loading.

ARTICLE HISTORY
Received 22 May 2023
Accepted 16 April 2024

KEYWORDS
Particle tracking; accelerated pavement test; MLS11; profilometer; displacement field

1. Introduction

Pavement performance is quantified by the period of time over which a given volume of traffic can be provided with an acceptable level of service by the road. The concept of acceptable levels of serviceability can be traced back to AASHO (American Association of State Highway Officials) road tests conducted in the 1960s. The Present Serviceability Rating (PSR), developed during these road tests, is a direct, subjective measure of the level of service offered by a road at any given time. Since then, the evaluation of serviceability has moved from subjective measures (such as PSR) to more quantifiable objective measures such as the Pavement Serviceability Index (PSI), which is a function of measurable quantities including slope variance, length of cracking and surface rutting. PSI has been widely adopted as the measure of pavement performance since its inclusion in the AASHTO (American Association of State Highway and Transportation Officials) 1993 Pavement Design Method. Today, the Mechanistic-Empirical Pavement Design Guide (NCHRP 2004), developed by AASHTO, involves designing pavements using limits on the various parameters that govern PSI, namely rutting and cracking.

The aforementioned methods evaluate changes in serviceability as a function of surface conditions. However, distress at the pavement surface is merely a symptom of the overall response within the pavement structure. As an example, while rutting is measured at the pavement surface, the total deformation at the surface is the cumulative sum of the change in thickness due to compression and lateral movements of the various underlying pavement layers. Similarly, while fatigue cracking is observed at the surface, the development of such cracks is directly related to the elastic tensile strains induced due to vehicular traffic load at critical locations within the asphalt layers. Thus, to improve pavement performance, the internal response of the pavement structure to external influences, such as environmental conditions and traffic loads, must be quantified and linked to the as-built characteristics of the pavement such as the modulus and thickness of its various layers. For instance, it can be hypothesised that restricting the internal movement of particles would also restrict the compression and lateral movement of internal layers, thereby reducing surface rutting. Accordingly, restricting internal movements to control surface rutting would require knowledge of the location, magnitude, and direction of such movements. Furthermore, monitoring the internal movement of particles could provide insight into the internal mechanisms that the road undergoes under external loads.

Although modern design methods and pavement evaluations consider internal stresses, strains and displacements in their methodologies, these internal parameters have been assessed primarily by predicting them through analytical (layered elastic analysis) or numerical (finite element or finite differences methods) means. While localised measurements of stresses and strains have been collected in some pavement studies via earth pressure cells and strain gauges, they employed expensive, single-use sensors that precluded obtaining comprehensive internal stress–strain distribution profiles. This is especially true when measuring strains/displacements within a pavement system, as continuous profiling may require a network of daisy-chained strain gauges that are not only cost-prohibitive but also intrusive, therefore possibly interfering with the pavement response being quantified.

CONTACT S. Subramanian ssubu.ind@utexas.edu

This paper describes the pilot study of a broader research program aimed at understanding the internal mechanisms associated with stabilisation of unbound aggregate bases by geogrids. In flexible pavements, one of the primary mechanisms hypothesised to be associated with geogrid stabilisation is 'lateral restraint' whereby the geogrid restrains the horizontal movement of the aggregate particles in the immediate vicinity of the geogrid (Sun and Han 2019). The objective of the pilot study is to develop a cost-effective, novel method that can quantify the lateral restraint provided by a geogrid through the measurement of internal horizontal particle movements within the unbound aggregate layers of a pavement structure. The method discussed herein combines mechanical extensometers used to monitor displacements in structures such as slopes and earth-retaining structures in the field (e.g. Zornberg *et al.* 1995) with low-cost external linear position transducers that accurately record the position of tell-tales. Further, the outcome of the pilot study is used to determine the feasibility of using tell-tales to measure lateral restraint and to assess their viability for use with full-scale pavement sections in the field. The externalisation of the sensors, when used in field pavements sections, should facilitate their recovery and reuse after the completion of the project. Only the tell-tales, themselves, are lost to the structure of the test sections, and these can be economically replaced. In addition to the particle tracking system, the pavement structure tested in this study was monitored using a 2D laser profilometer, also developed as part of this study to measure surface rutting as well as earth pressure cells to measure the stress distribution within the pavement structure.

2. Materials and methods

2.1. Pavement layers

The reduced-scale pavement structure constructed for this study consisted of a 150-mm sand subgrade layer, 125-mm gravel base layer and 25-mm Hot Mix Asphalt (HMA) ride surface. The entire structure was built above grade in two modular frames, each measuring 150 mm in height, to facilitate access to the sensors from the sides of the frame. The pavement structure was 1800 mm in length, 1200 mm in width and had a total depth of 300 mm, as shown in Figure 1. The length of the pavement structure was chosen to accommodate the trafficking equipment which has a trafficking length of 1100 mm with a buffer of 350 mm on each end. For the test width, the internal particle displacements on a wider test section (1800 mm) were measured and the distance from the wheel path at which particle displacements became zero was used (with a buffer of 150 mm) to determine the required test width to mitigate the effect of boundary conditions. A lightweight non-woven geotextile with very low tensile strength was used for separation between the base and subgrade. A clean, uniformly graded sand with a D_{50} of 0.5 mm and specific gravity of 2.655, commercialised as Monterey 0/30 sand, was used as the subgrade. It classified as a poorly graded sand (SP) with a Coefficient of Uniformity (CU) of 1.8 and a Coefficient of Curvature (CC) of 1.0. The subgrade was placed in three lifts of 50 mm each, reaching a total thickness of 150 mm. This thickness is determined to be adequate for distributing the applied vertical stress to less than 5% at the bottom of the subgrade. The subgrade lifts were compacted via hand tampers to a dry unit weight of 15.4 kN/m^3, corresponding to a relative density of 67%. The base layer consisted of a clean, uniformly graded, river-washed gravel with a D_{50} of 7 mm and a specific gravity of 2.650. The base material conformed to AASHTO #8 gradation and classified as a poorly graded gravel (GP), with a CU of 1.6 and CC of 1.0. The base was placed in four 25-mm lifts and two 12.5-mm lifts, reaching a total thickness of 125 mm. The lifts were compacted via hand tampers to a dry unit weight of 17.1 kN/m^3, corresponding to a relative density of 85%. The pilot study described in this paper is used to establish a baseline (control) against which other identical pavement sections differing only in the type of geogrid can be compared. In order to improve repeatability and consistency across all the pavement sections, a uniformly graded base and subgrade without fines is used. This mitigates the variation in in-situ density and modulus of the pavement layers by removing the effect of moisture content (no fines) and compaction effort (uniform gradation). The asphalt mixture used for the surface layer was a Thin Overlay Mix (TOM) (class A), which conformed to TxDOT Special Specification 3239 (TxDOT SS3239 2004) and had a binder content of 6.5%. The thickness of the base and asphalt surface

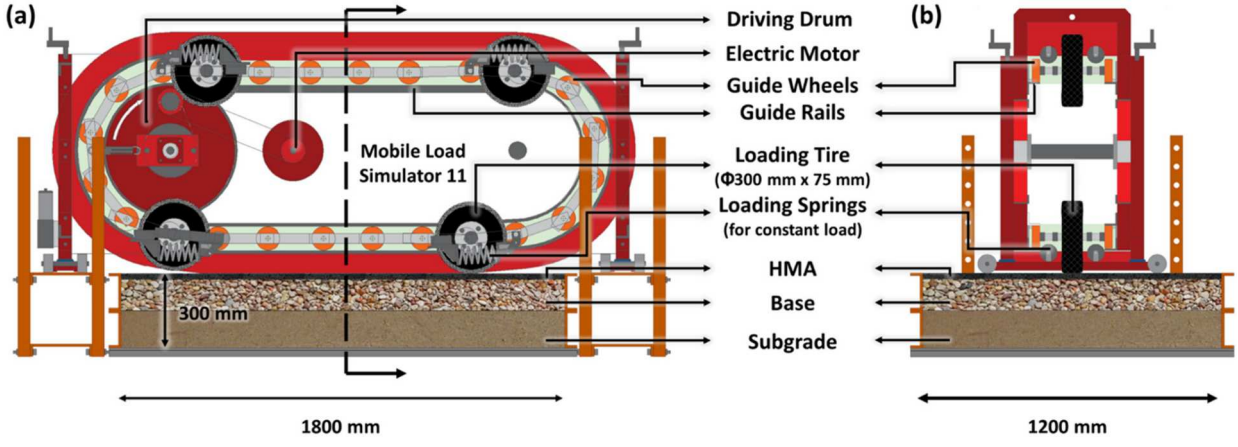

Figure 1. Schematic of pavement cross-section with MLS11: (a) longitudinal; and (b) transverse.

layers are chosen to represent a typical flexible pavement configuration with a thickness ratio of 5:1 used for rural highways.

2.2. Trafficking equipment

A model Mobile Load Simulator [MLS11, previously referred to as MMLS (Kim *et al.* 1998, J. Lee *et al.* 2006)] was used to traffic the pavement sections. It consists of four loading tires connected to a chain of guide wheels that are guided along rails in a vertical obround path. The chain of guide wheels is propelled by a driving drum connected to an electric motor. This system allows repeated, unidirectional, rolling wheel loads of 2.1 kN at tire pressures of 620 kPa to be applied to the pavement surface over a track length of 1.1 m. The MLS11 is lowered onto the pavement surface using four positioning screws at the ends while a loading spring and hinge mechanism attached to each loading tire ensures the applied load remains constant with surface deformations (up to 12 mm). Table 1 provides further technical specifications of the loading equipment.

The MLS11 was originally developed in a pilot study, as a reduced-scale model of the full-scale accelerated pavement testing devices such as the MLS30 and MLS66 (van de Ven and Smit 2000). Because of its reduced-scale, the MLS11 has a smaller tire footprint (contact area) compared to the full-scale load simulators and hence a reduced depth of influence of the applied load. Therefore, the MLS11 was predominantly used to evaluate the surface layer of full-scale flexible pavements in the field and for comparisons against full-scale vehicular load simulators (Walubita 2000, Walubita *et al.* 2000, Epps *et al.* 2001, Martin *et al.* 2003, Smit *et al.* 2003, 1999, Gehrig *et al.* 2010). These field sections were predominantly non-instrumented, and their performances were primarily evaluated through the surface distress development such as rutting. In the laboratory, the MLS11 has been used to determine and validate the performance of bituminous mixtures through the construction and trafficking of asphalt concrete slabs over an elastic medium such as polymeric foams or neoprene rubber (Lee and Kim, 2004, S. J. Lee *et al.*, 2006, Bhattacharjee and Mallick 2012). The asphalt slabs in these studies were typically instrumented with strip-type strain gauges to measure the elastic and plastic tensile strain development under the wheel path. This information was used to evaluate the rutting and fatigue characteristics of the various HMA mixtures used in these studies. Kim *et al.* (2009) used the MLS11 to run accelerated pavement tests on asphalt slabs reinforced with carbon FRP (Fiber Reinforced Plastic) supported on cellular rubber pads. The asphalt slabs were instrumented with strain gauges which showed a 10–15% reduction in tensile strains in the transverse and longitudinal directions in the slabs reinforced with carbon-FRP. Lee *et al.* (2015) evaluated the performance of geosynthetic-reinforced asphalt slabs supported on top of a rigid steel plate. The mechanisms of shear flow associated with lateral movement of the pavement layers were observed under the MLS11 loading demonstrating the ability of the MLS11 loading to capture mechanisms associated with pavement surface deformations. Limited research is available on the use of MLS11 to evaluate the performance of the base and subgrade layers of reduced-scale pavement structures. Tang *et al.* (2008) performed accelerated pavement tests on reduced-scale pavement sections consisting of the subgrade, base and HMA surface layers. The performance of the various sections was evaluated through surface profiling in order to determine pavement ruts with increasing traffic cycles. Reduced-scale pavement sections (with subgrade, base and HMA layers) with instrumentation to measure the elastic subgrade deformations under the rolling wheel load and the cumulative subgrade rutting were studied by Tang *et al.* (2014). The instrumented setup consisted of an LVDT to measure the subgrade deformation and foil-type strain gauges to measure strains in the stabilising geogrid. A rigid pavement structure consisting of disjointed concrete slabs, on top of a silty aggregate sub-base and a non-plastic silty subgrade was trafficked using the MLS11 by Kermani *et al.* (2018) in order to study the fines migration and pumping commonly observed in full-scale rigid pavements. The pavement response, in terms of internal stress distribution at the Sub-base:Subgrade interface, and the pore water pressure within the subgrade were monitored using earth pressure cells and piezometers, respectively. A review of the available literature showed no studies that report the instrumented response of the aggregate base in reduced-scale pavement sections under accelerated pavement testing under MLS11.

Table 1. Relevant technical specifications of MLS11 equipment used in this study.

Property	Specification
No. of loading tires	4
Wheel diameter	300 mm
Tire width	80 mm
Total track width	80 mm
Total track length	1100 mm
Load per wheel	2.1 kN
Tire contact pressure	620 kPa
Tire footprint area	34 cm^2
Loading rate	120 passes per minute
Wheel velocity	2.5 m/s
Lateral wander	Disabled

2.3. Instrumentation

The instrumentation used to monitor the performance of the pavement sections included a 2D surface profilometer to measure the surface rutting of the pavement structure, earth pressure cells to measure the vertical stress under the wheel load at specific locations within the pavement structure, and artificial particles to facilitate tracking the horizontal movement of particles within the base layer.

2.3.1. Profilometer

An industrial 2D laser from Micro-epsilon (model LLT2500–100) was used to develop a profiling system suitable to capture surface deformations. This laser is capable of scanning up to 300 profiles per second, with each profile consisting of roughly 640 points distributed over a width of 100 mm (roughly one sample point for every 150 microns). This laser was mounted on a glide cart that glides back and forth along a linear belt-driven actuator (Macron Dynamics Part: MSA-PSC-O-GB-AM3–2000). The actuator consists of a 2.4-m-long extruded

aluminum section, with a maximum travel length of 2.06 m, driven by an integrated stepSERVO™ motor (Applied Motion Products TSM23Q-2RG) capable of displacing the profiling laser at variable speeds of 1 to 1200 mm/s. Two inductive proximity sensors are used as hardware end limit switches on either ends of the actuator resulting in 2 m of usable travel. These limits may be further adjusted based on the width of the test sections by either physically moving the end limit switches or setting up software end limits through the stepSERVO™ Quick Tuner software. For the purposes of this study, the actuator operated at 25 mm/s with the laser scanning 25 profiles per second, resulting in a sampling frequency of one profile per mm of pavement section.

Pavement surface profiling was completed pre-trafficking before testing commenced, at pre-determined intervals during trafficking, and post-trafficking after pavement failure. To determine the progression of the surface rut with an increasing number of wheel passes, trafficking was interrupted at pre-determined intervals (after 100, 1000, 3000, 10,000 and 20,000 passes from the start of testing), the MLS11 was removed from the pavement section, and the pavement surface was profiled along four different locations as depicted in Figure 2. Thus, a complete pavement profile consisted of one longitudinal profile (labelled 'Long' in Figure 2) along the path of trafficking, and three transverse profiles (labelled 'Begin', 'Center' and 'End' in Figure 2) perpendicular to the direction of trafficking, each spaced 250 mm apart.

2.3.2. Earth pressure cells

The earth pressure cells selected for this study were KDC and KDE sensors from Tokyo Measuring Instruments Lab (TML), rated for 500 and 200 kPa vertical compressive stress. These sensors are 350 Ω full-bridge strain-gauge-based pressure cells that were designed to be embedded within the soil. Eight sensors were used within the pavement section to capture the vertical stress distribution. The three larger KDC sensors were placed near the mid-depth of the base layer. Three of the five smaller KDE sensors were placed at the base-subgrade interface beneath the non-woven geotextile while the remaining two were placed at the bottom of the subgrade. Figure 3 displays the layout of all eight earth pressure cells within the pavement structure. The sensors were staggered to avoid being installed atop one another to prevent local stiffening given the pavement layer thicknesses and profile of the sensors. Figure 4 shows the KDE pressure cells installed on top of the subgrade with a biaxial level to ensure that the sensors are vertical.

2.3.3. Particle tracking sensors

Pavement surface rutting may result from the movement of particles within the various pavement layers. This mechanism has been recognised in modern mechanistic design methods wherein the surface rut is computed as the arithmetic sum of the rutting contributions by the individual pavement layers (NCHRP 2004). From the mechanistic point of view, the component of the rut attributed to the unbound aggregate base can be classified into two types: (1) one-dimensional densification of the unbound pavement layer under wheel loads, and (2) lateral flow due to incremental shear of the pavement layers with repeated traffic passes. For an adequately compacted unbound aggregate layer, the component of rutting due to densification can be considered negligible. Thus, for well-compacted unbound aggregate layers, any vertical settlement under wheel loads attributed to the base layer must be accompanied by a corresponding lateral flow or horizontal displacement of the aggregate particles. Observing the lateral displacement of particles under trafficking is expected to provide significant insight into the development and progression of rutting in unbound aggregate layers.

In this study, the lateral movements of aggregate particles induced by wheel passes were monitored using a unique setup that combined mechanical extensometers, typically used in field embankments to monitor soil movement, with linear displacement sensors. This setup consists of artificial particles embedded within the soil matrix and tied to tell-tale wires spanning the pavement structure, the other ends of which are connected to linear position transducers mounted outside the pavement structure. As a result, any particle movement within the base is transferred through the tell-tale wires

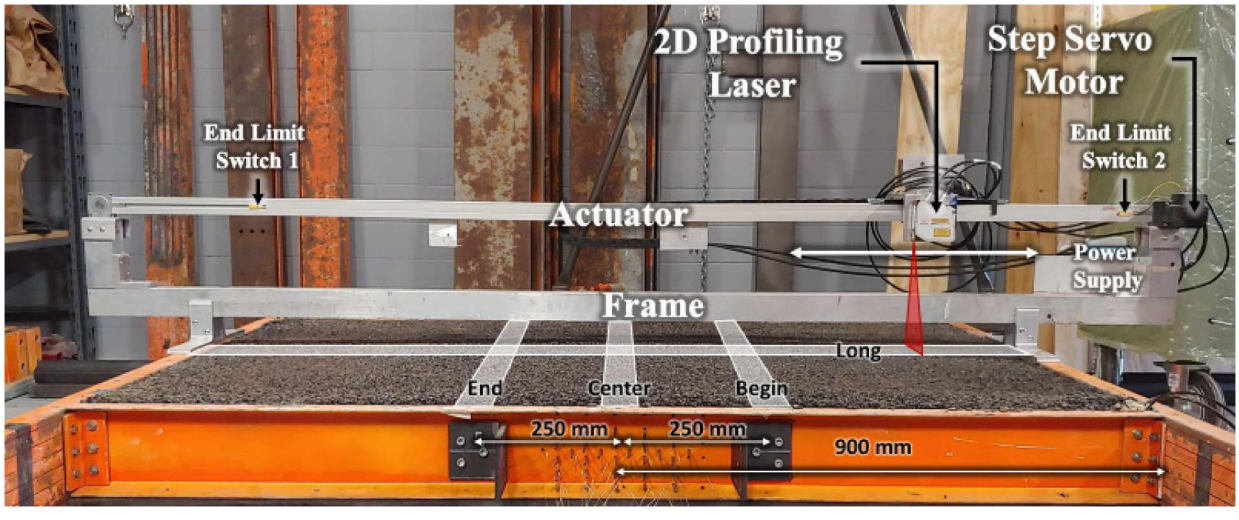

Figure 2. Assembled laser profilometer.

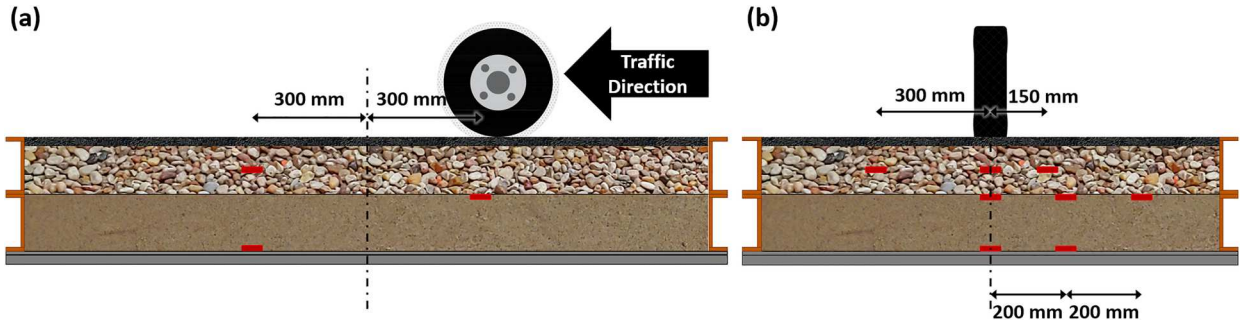

Figure 3. Pressure cell layout: (a) longitudinal cross-section; and (b) transverse cross-section.

to the position sensors on the sides of the pavement structure. An alternative method to track the particle movement in unbound aggregate layers would be the use of SmartRock sensors (Liu *et al.* 2015). However, at the time of this research SmartRock sensors were not commercially available, specifically at the particle size of the aggregates in the base layer used in this study.

The artificial particles were fabricated using a 9-mm-long, 6.5-mm-wide stainless-steel hex bolt (8–32 thread) and a 6.5-mm-wide, 2.5-mm-thick hex nut. The final profile of a fully assembled artificial particle comprises a 6.5-mm-wide, 5-mm-tall hex-head with a 4-mm-wide, 4-mm-tall threaded base (Figure 5a). The following steps were taken to improve the interaction between the artificial particles and the surrounding aggregate particles: (1) the final profile of the artificial particles was selected to correspond closely to the D_{50} of the base material (7 mm); (2) the hex nuts and bolts were chosen due to their shape with sharp edges and threaded base; (3) the polished surfaces of the hex nuts and bolts were sanded with a coarse-grit sandpaper; and (4) the particles were installed with the axis of the bolt-nut assembly perpendicular to the direction of the tell-tale.

A total of 30 artificial particles were installed within the base, forming a dense array of trackable particles as displayed in Figure 6. They were installed in six layers at a vertical spacing of 25 mm, with five sensors per layer located 75, 150, 225, 300, and 450 mm laterally away from the location of the wheel path. Since each artificial particle was connected to a linear potentiometer outside the pavement structure, the five sensors installed at the same depth in each layer were staggered 50 mm from each other longitudinally.

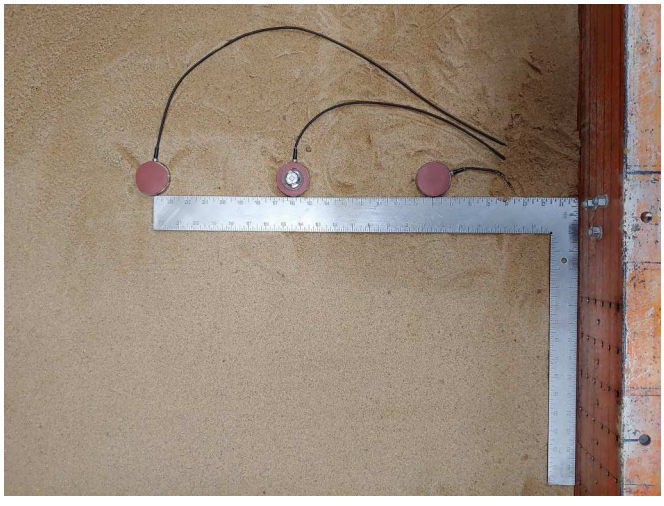

Figure 4. KDE pressure cells installed on top of subgrade.

Spring-back 316 stainless steel wire 0.5 mm in diameter was utilised for the tell-tale wires. These wires were looped between the nut and bolt of the artificial particles and held in place by 20–24 AWG wire ferrules crimped next to the bolt thread. The nut and bolt assemblies were also fastened to prevent any play between the tell-tale wires and artificial particles. The tell-tale wires were routed from the artificial particles located within the base to the displacement sensors located outside the pavement structure, at the sides of the modular frames. Excluding the first 40 mm from the particle, the entire length of the tell-tale wires was protected against possible damage using high-performance bicycle brake housing as a sleeve (Figure 5b). The first 40 mm remained exposed to allow for particle movements toward the edge of the pavement structure.

The unique construction of the particle tracking system is aimed at mitigating the influence of the sleeves/wires on the measured strains. The wires and sleeves were chosen to have a minimum radius of curvature that accommodated the vertical deformation of the unbound aggregate layer without offering resistance. The housing sleeve contains a Teflon-lubricated inner liner tube to reduce any friction against the sliding of the tell-tale wires to facilitate an accurate no-ply transfer of particle movement to the outside of the pavement. The liner tube is encased within the walls of the middle coiled high-carbon steel, which protects the tell-tale wires against pinching, bending and other damage from the surrounding aggregate particles. The coiled steel is covered in a polymeric outer layer to mitigate the resistance to horizontal particle flow near the housing.

The free ends of the tell-tale wires were connected to an eye fitting on the linear position transducers mounted outside the pavement structure, which measure the lateral movement of the artificial particles (Figure 5c). The linear position transducers from Unimeasure (LX-PA Series) are ratiometric sensors that output a fraction of the input excitation voltage according to the position of the potentiometer using a voltage divider circuit. These analog sensors divide a 1000 Ω potentiometric circuit over a range of ± 25 mm with a high degree of linearity (1% full-scale). In theory, the analog nature of these sensors allows for infinite resolution in the measured position, however in practice the resolution is limited by the noise level associated with the data acquisition system. For the system

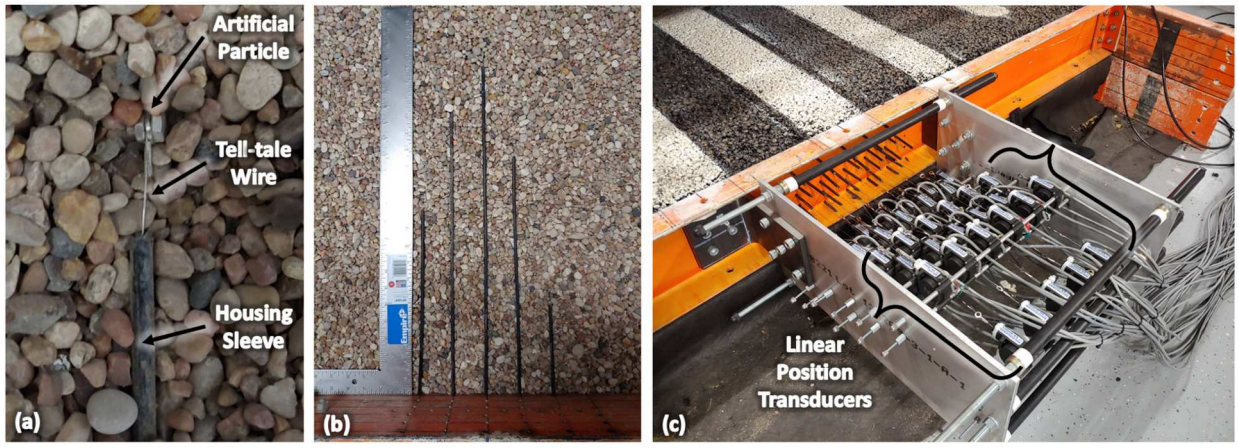

Figure 5. Particle tracking assembly (a) artificial particle connected to tell-tales; (b) housing sleeves run from artificial particles to outside of box; and (c) linear position transducers mounted onto overhanging frame.

used in this study (National Instruments USB-6255), the resolution in displacement measurement is estimated to be 2 microns with an absolute accuracy of 14 microns at the full-scale. Since the minimum horizontal spacing between any two sensors is 75 mm, the smallest change in strain detectable by the system is 26.7 micro-strains with a relative accuracy of 0.2% which is sufficient to measure the permanent strain changes expected in a typical flexible pavement. Figure 5c shows the frame, designed to hold over 30 sensors in a tight matrix over the edge of the pavement, to which these sensors were mounted.

3. Results and discussion

This section details the response of the pavement test section to trafficking by the MLS11 with no lateral wander. The pavement section was subjected to 20,000-wheel passes while the vertical stress distribution within the pavement structure and horizontal particle movements in the base layer were continuously measured. Trafficking was briefly interrupted after 100-, 1000-, 3000-, and 10,000-wheel passes to measure surface deformations using the profilometer. The initial and final surface profiles were also determined before and after the end of the trafficking cycles.

3.1. Surface rutting

Figure 7 shows the centre rut profile of the pavement section after 10,000 passes, determined by subtracting the initial centre-transverse profile from that obtained after 10,000 passes. Figure 7a shows the profile measured by the laser profilometer as a 2D contour plot. The x-axis corresponds to the transverse distance from the centre of the wheel path of the laser as it was guided across the pavement section when measuring the surface profile. The y-axis provides the lateral distance from the centre of the laser perpendicular to the direction of motion. The darker centre region (in blue), around 0 mm in the transverse direction, represents the area that is deeper than in the initial profile, which corresponds to the wheel path. The adjacent darker regions (in red), around ±200 mm, represent the areas that are shallower than in the initial profile, which correspond to the heave on either side of the wheel path. The lighter region between the darker red and darker blue regions shows the location of zero vertical deformation, or pivot point, around which the pavement surface deforms. The development of rut from a depression along the wheel path accompanied by shear upheavals on either side of the wheel path is known to be associated with the lateral flow of materials in the pavement layers (NCHRP 2004).

The measured profile contains high-frequency noise due to laser reflections from the sharp edges of the particles in the HMA surface. To remove this noise, the measured profile was filtered using a low-pass, 5th order Butterworth filter with a cut-off frequency of 0.035 samples/mm along both axes. Figure 7b shows the filtered surface profile. The filtering attenuated the noise by 99% or more for particle sizes up to 10 mm, which is the maximum aggregate size used in the TOM-A mix of the HMA layer.

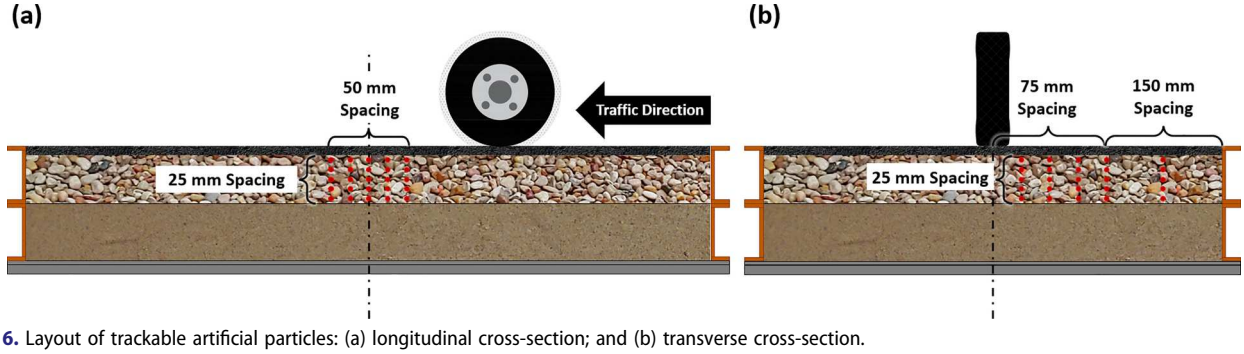

Figure 6. Layout of trackable artificial particles: (a) longitudinal cross-section; and (b) transverse cross-section.

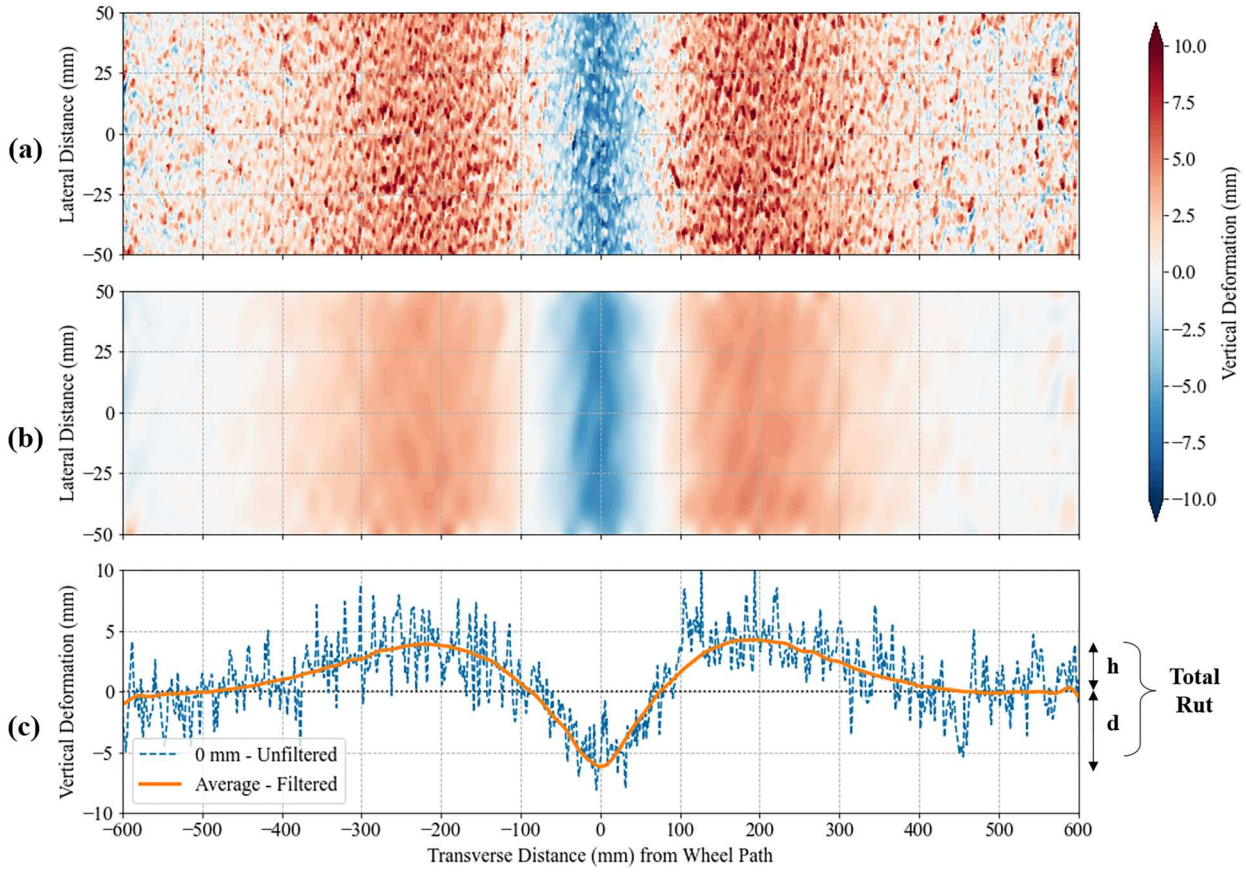

Figure 7. Transverse profile after 10,000-wheel passes: (a) raw 2D contour; (b) filtered 2D contour; and (c) 1D profile.

In addition to these reflection artifacts, the overall surface texture of the HMA surface also introduces some particle shape noise into the profiles. To remove the noise due to individual particles, the average transverse profile for the 100-mm lateral distance scanned by the laser was determined as indicated by the solid orange line in Figure 7c. This is the same data shown in Figure 7b but averaged along the lateral direction (y-axis). The dashed blue line in Figure 7c corresponds to the transverse profile measured at the centre of the laser (0 mm lateral distance) before filtering. The process of averaging removed the noise due to individual particle shapes and also allowed for small errors in the lateral placement of the profilometer during profiling after various numbers of wheel passes, resulting in a clean rut profile.

Figure 8 shows the average profiles obtained at the transverse profile location 'Center' at increasing number of wheel passes. The rut progression is primarily driven by the lateral flow of base material through shearing as evidenced by: (1) the increase in heave next to the wheel path proportionate to an increase in the depression along the wheel path; and (2) the location of the transition from depression to heave remaining at a constant distance (around ±80 mm) from the centre of the wheel path. From the average profiles, the total rut at the centre of the pavement section is determined as the sum of the vertical depression depth (d) under the wheel path and corresponding heave (h) adjacent to the wheel path, as shown in Figure 9.

The ruts are also measured at two other transverse profile locations, 'Begin' and 'End', which are 250 mm on either side of the 'Center' location. The rut measured at all three locations and their average are given in Figure 10. The rut measured at the centre of the trafficked length is very close to the average of all three locations. In contrast, the ruts measured at 'End' are higher than the average and those measured at 'Begin' are lower than the average by less than 15%, which is considered acceptable for the purposes of this study.

3.2. Subsurface displacements

As previously described, the particle tracking sensor is a flexible, protected tell-tale wire connected to an artificial particle within the pavement structure on one end and to a linear position transducer on the other end. The flexible nature of the system accommodates possible vertical movements of the pavement layers without significantly affecting the measurement of horizontal displacements. An upper bound on the measurement error due to potential vertical movements of the pavement layer can be obtained by considering the vertical movements as measured by the profilometer at the surface. It is assumed that the vertical movement of pavement layers beneath the surface results in a final subsurface profile with a larger radius of curvature (i.e. is straighter) than the surface profile. Figure 11 illustrates the case of a particle located on the surface at the centre of the wheel path (dashed square). Theoretically, this particle will undergo a maximum vertical displacement with zero horizontal displacement to reach its final position (solid square). As a result, a tell-tale wire running

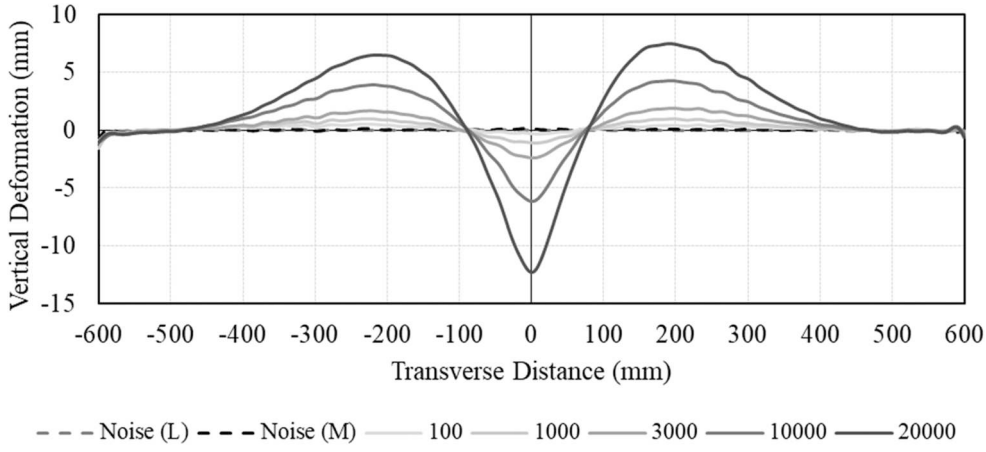

Figure 8. Rut profiles with increasing number of wheel passes.

from this particle to the edge of the pavement would measure only the error due to the vertical displacement. Since the particle does not undergo any horizontal displacements, the vertical displacement of the pavement layer would result in an increased wire length within the pavement. Thus, the overhanging portion of the wire outside the pavement is reduced in length by ΔL, which equals the difference in the length of the surface deformation profile before and after the vertical displacement. Therefore, the error due to vertical displacements is always registered by the linear position sensor as if the particle moved toward the centre of the wheel path (negative displacement by convention).

By calculating the length of the vertical displacement curve (i.e. surface profile) from the centre of the wheel path to the edge of the pavement, and comparing it to the original length before trafficking, the maximum error in horizontal displacement measurements due to vertical displacements can be determined. Table 2 summarises the maximum error in horizontal displacement measurements at increasing number of passes. As can be seen in the table, the maximum error calculated at the end of the test (after 20,000-wheel passes) is less than 1.5 mm, which is about 10% of the vertical displacement under the wheel path. This is the maximum possible error in the horizontal displacement measurement for a particle on the surface of the pavement located at the centre of the wheel path. For particles within the pavement and away from the wheel path as shown in Figure 6, the error in horizontal displacement measurement is expected to be significantly smaller.

Considering that the subsurface profiles have a larger radius of curvature than the surface profile, a lower bound for the minimum radius of curvature of the layers within the base can be determined. The radius of curvature along the surface profile is determined from the first and second derivatives of the profile. From the surface profile obtained after 20,000 passes, the minimum radius of curvature was found to be 70 mm at the centre of the wheel path. The tell-tale wires and housing sleeve were chosen such that their minimum radii (25 and 50 mm, respectively) were smaller than the minimum radius of curvature required (70 mm), allowing them to be flexible enough to accommodate the subsurface profile movements.

Figure 12 shows the cumulative displacements after 10,000 passes measured by the particle tracking sensors at six different depths within the base and five different transverse distances from the wheel path. The transverse horizontal displacement under the wheel path is zero due to the symmetry of displacements across the wheel path. At 600 mm from the wheel path,

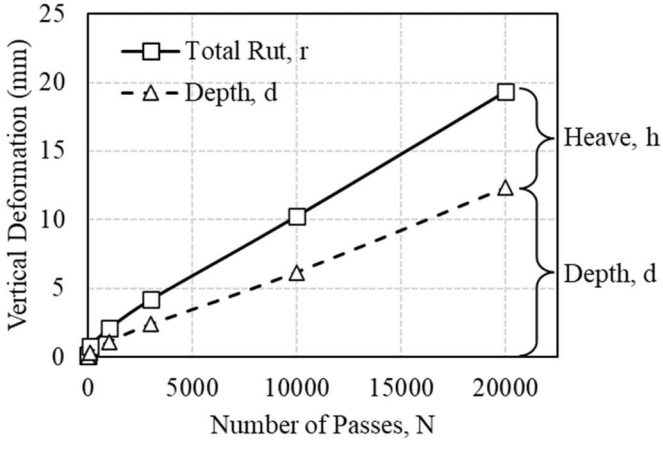

Figure 9. Rut, heave, and depression depth as a function of number of passes, *N*.

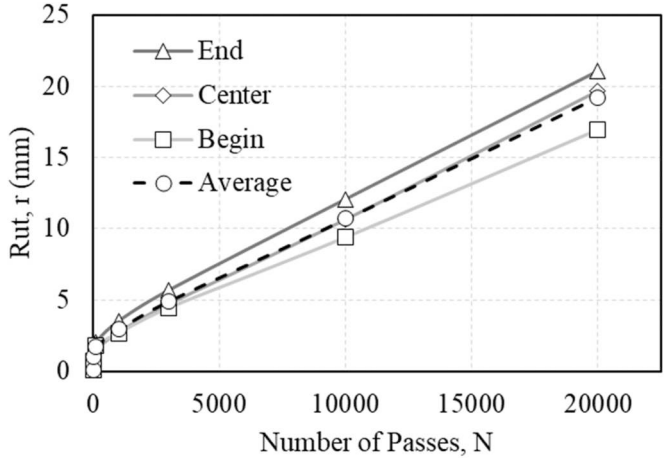

Figure 10. Rut vs. number of passes along pavement section.

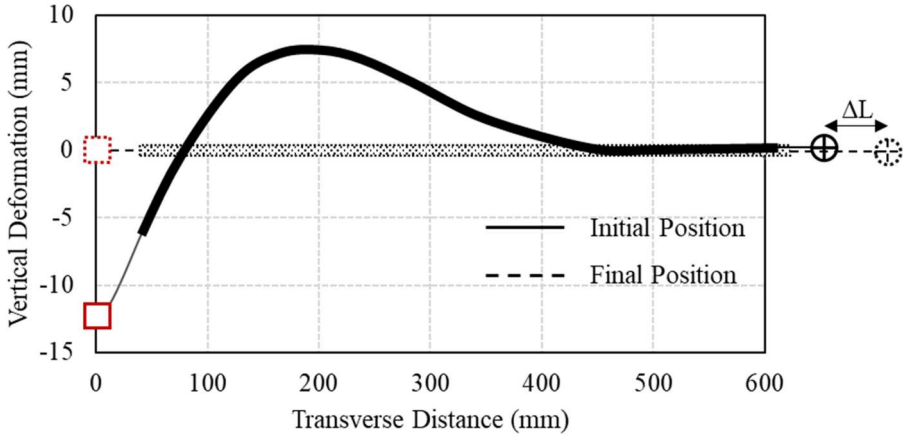

Figure 11. Measurement error due to vertical displacement at surface.

the transverse horizontal displacement is also zero since this is the edge of the pavement section bounded by steel channels.

To interpolate the horizontal displacement data along the transverse direction from the wheel path, the five measured transverse displacements at any particular depth and two transverse displacements determined from the boundary conditions were fitted with a function, as indicated by the solid lines in Figure 12. The best-fit function representing the cumulative horizontal displacements must have properties that capture the behaviour of the particles in the base under trafficking. Therefore, the function chosen to fit the transverse displacement data should:

(1) be equal to zero at the origin (wheel path), where the horizontal displacement is zero due to symmetry.
(2) be an 'odd' function, i.e. symmetric about the origin (wheel path), so that the transverse horizontal particle displacements are symmetric about the wheel path but reversed in direction on either side of the wheel path.
(3) monotonically increase to a maximum at a given distance from the wheel path (region of tensile strains around the wheel path) and then asymptotically decreases to zero at infinity (region of compressive strains away from the wheel path).

Among the several functions considered for fitting the transverse displacement data, the following function satisfies the above characteristics and best fit the measured data:

$$u = Axe^{-Bx^2} \tag{1}$$

Table 2. Maximum error in horizontal displacements due to vertical settlement.

Number of passes N	Surface profile length $2L$ (mm)	Maximum error ΔL (mm)	Vertical depression depth d (mm)	Percentage of vertical displacement $\Delta L/d$ (%)
0	1200.00	0.00	0.0	0.0%
100	1200.05	−0.03	0.4	7.8%
1000	1200.11	−0.05	1.1	4.8%
3000	1200.16	−0.08	2.4	3.4%
10,000	1200.83	−0.42	6.2	6.7%
20,000	1202.82	−1.41	12.3	11.4%

where u is the transverse horizontal displacement away from the wheel path; x is the transverse distance from the wheel path; and A & B are fitting parameters greater than zero.

Particle displacements at six different depths within the base layer were fitted with the function in Equation (1). The best-fit parameters, A and B, after 10,000 passes for each depth, z, are shown in Figure 13. The parameter A decreases approximately linearly with increasing depth, while the parameter B increases in a log-linear fashion with increasing depth. The linear and log-linear functions that correspond to the best fit displacement data are shown in the figure. The transverse horizontal strains are obtained as the derivative of Equation (1), as follows:

$$\varepsilon_x = \frac{du}{dx} = A(1 - 2Bx^2)e^{-Bx^2} \tag{2}$$

where ε_x is the transverse horizontal strain (tension is positive).

Setting Equation (2) equal to zero, the location of peak displacement can be obtained as a function of parameter B as follows:

$$x_{peak} = \pm \frac{1}{\sqrt{2B}} \tag{3}$$

where x_{peak} is the location of the peak horizontal displacement from the centre of the wheel path. The magnitude of peak displacement is obtained by substituting Equation (3) into Equation (1):

$$u_{peak} = \frac{A}{\sqrt{2Be}} \tag{4}$$

where u_{peak} is the magnitude of the peak horizontal displacement. Figure 14 shows the location and magnitude of the peak horizontal displacements at various depths within the base layer after 10,000 passes. As expected, the peak displacement occurred in the layers closest to the surface and decreased with increasing depth. Interestingly, the location of the peak displacement approaches the centre of the wheel path with increasing depth. From Equations (3) and (4), the fitting parameters A and B can be expressed in terms of the location and magnitude of the peak horizontal displacement

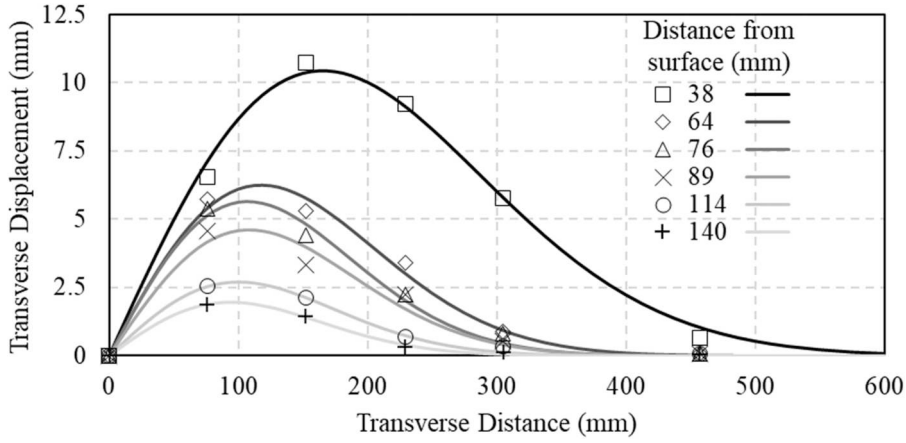

Figure 12. Cumulative particle displacements after 10,000 passes.

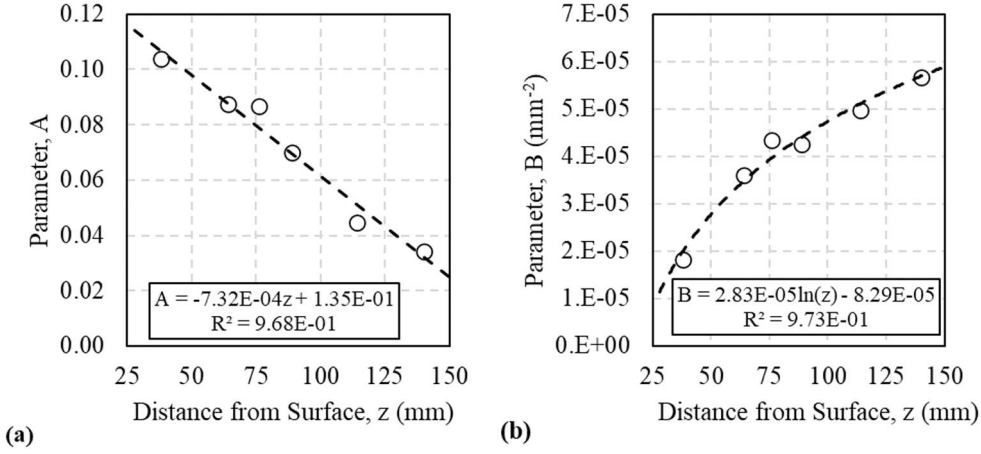

Figure 13. Fitting parameters vs. depth, z, after 10,000 passes: (a) parameter A; and (b) parameter B.

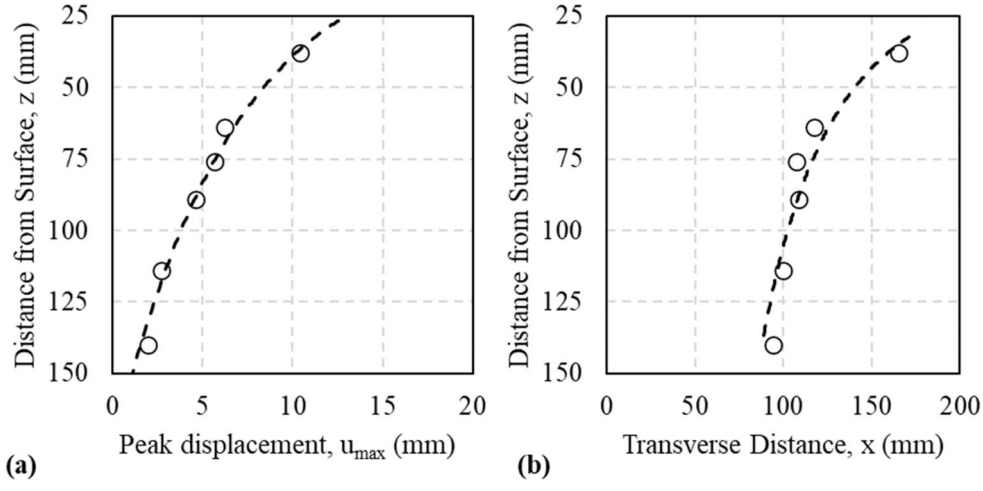

Figure 14. Peak displacement after 10,000 passes: (a) magnitude, u_{peak}; and (b) location, x_{peak}.

for a given depth within the base as follows.

$$A = \frac{u_{peak}}{x_{peak}}\sqrt{e} \tag{5a}$$

$$B = \frac{1}{2x_{peak}^2} \tag{5b}$$

From Equation (2), it can be inferred that the fitting parameter A corresponds to the maximum tensile strain under the wheel path (when $x = 0$). Thus, Equation (1) for the horizontal displacement [and (2) for tensile strain] can be redefined using the location and magnitude of the peak horizontal displacement [Equation (5)] as follows.

$$u = u_{peak}\left(\frac{x}{x_{peak}}\right)e^{\frac{1}{2}\left[1-\left(\frac{x}{x_{peak}}\right)^2\right]} \tag{6}$$

$$\varepsilon_x = \varepsilon_{o,\,peak}\left[1-\left(\frac{x}{x_{peak}}\right)^2\right]e^{-\frac{1}{2}\left(\frac{x}{x_{peak}}\right)^2} \tag{7}$$

where $\varepsilon_{o,peak} = A$ is the peak tensile strain under the centre of the wheel path.

From Figure 13, the fitting parameters A and B for the horizontal displacement function are determined for any depth within the base layer. Consequently, Equations (1) and (2), using the fitting parameters for a given depth, can be used to predict the horizontal particle displacements and tensile strains at any point within the base layer. This information was used to generate the horizontal displacement fields and tensile strain fields within the base layer with increasing number of wheel passes. Figure 15 presents the development of horizontal displacements with increasing number of wheel passes as contour plots. The x-axis of the contour plots corresponds to the distance from the wheel path in the transverse direction, with 0 mm at the centre of the wheel path and 600 mm at the edge of the pavement. The y-axis corresponds to the depth from the surface of the completed pavement section, with the HMA-base layer interface at 25 mm and the base-subgrade interface at 150 mm. The contours represent the horizontal displacements, with the darker regions corresponding to higher displacements. The displacement contours progress from near the HMA-base interface to the bottom of the base layer with increasing surface rut due to trafficking. Peak displacements occurred between 100 and 200 mm from the wheel path near the HMA-base interface. As surface rut increased, the contour level (shade of red) representing the highest displacement near the HMA-base interface became darker indicating an increase in displacement at this location. This resulted in a downward and outward movement of the pre-existing contours away from the HMA-base interface. The top-down progression of the horizontal displacement contours observed in this pavement implied that the displacement measured are always higher closer to the surface and decreases with increase in depth. Thus, an increase in surface rut is accommodated by the lateral flow of material in the base layer, leading to the transfer of shear from the sub-layer near the top of the base to the sub-layer below, and from that sub-layer to the next, and so on, resulting in decreased displacements with increasing depth within the pavement structure. The data provides direct evidence of rutting caused by the lateral flow mechanism, as further substantiated by: (1) the accompanying heave adjacent to the wheel path in the surface deformation profiles (Figure 8); and (2) the essentially linear progression of rut and heave with increasing number of wheel passes (Figure 9), corresponding to the secondary phase of rutting with little to no volume changes (NCHRP 2004).

Figure 16 shows the vertical gradient of horizontal displacements as contour plots with increasing trafficking cycles. The vertical gradient is a measure of one of the two components of the shear strain within the base and represents the efficiency of the shear transfer from one sub-layer of the base to the adjacent sub-layers. Light contour levels represent regions with a comparatively low vertical gradient in horizontal displacements, i.e. movement of any particle in this region is accompanied by a movement of the same degree of the vertically adjacent particles (high shear transfer efficiency). Darker contour levels represent regions with a comparatively high vertical gradient in horizontal displacements, which implies a region with low shear transfer efficiency, i.e. movement of a particle in this region does not significantly affect the vertically adjacent particles. In the initial phases of trafficking, no significant vertical gradients were observed within the base layer, which corresponds to the initial phase of rutting with minimal shear development. The results indicate that increasing surface rut resulted in an overall increase in the vertical gradient of horizontal displacements. This effect was more prominent near the HMA-base interface at the location of the heave in the surface deformation profiles (Figure 8). The base aggregates closer to the HMA-base interface experienced larger lateral flow relative to the aggregates deeper within the base due to loss of confinement from the heave on the surface, resulting in reduced shear strength closer to the surface than deeper within the base. As the base aggregates towards the surface displaced laterally, the aggregates deeper within the base developed lateral displacements through the transfer of shear, the efficiency of which increased with depth. Thus, the difference in horizontal displacements between base aggregates with change in depth was more likely to be smaller at deeper depths than at shallower depths, as seen in Figure 12 (the difference in displacements between sensors at depths of 38 and 64 mm is greater than that between 114 and 140 mm).

The horizontal tensile strains within the base with increasing trafficking are presented as contour plots in Figure 17. The red contours correspond to regions of tensile strains (positive) while the blue contour levels represent regions of compressive strains (negative), with darker shades representing higher strain levels (tensile or compressive depending on the colour). In order to visualise the progression of horizontal normal strains through the unbound aggregate layer, a common scale is adopted for the sequential plots depicting the strain state with increasing number of passes. The discrete contour interval is chosen to be 2%. Tensile and compressive zones within the strain field are clearly demarcated by the white (lightest) contour level (denoting near 0% strain). The tensile

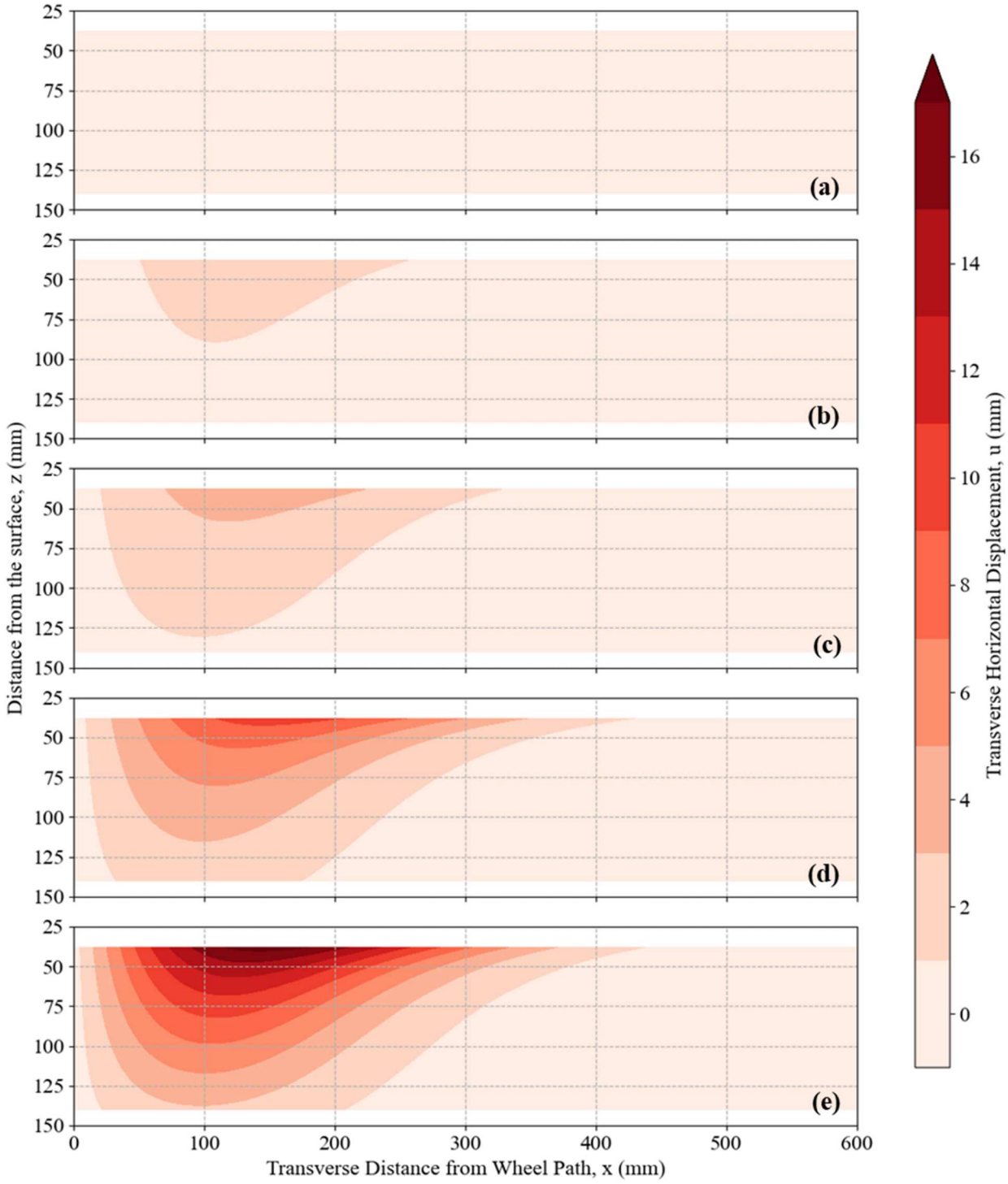

Figure 15. Cumulative horizontal displacements (mm) after: (a) 100; (b) 1000; (c) 3000; (d) 10,000; and (e) 20,000 passes.

zone occurs in the vicinity of the wheel path, with the maximum tensile strain occurring near the surface (y = 38 mm) at the centre of the wheel path (x = 0 mm). Cumulative compressive strains developed away from the wheel path, after a zone of zero strain (white contour level), corresponding to the location of maximum displacement. Maximum compressive strains developed away from the wheel path, between 150 and 250 mm, near the location of the heave in the surface deformation profiles (Figure 8). The compressive zone is followed by a zone of undisturbed base with zero strains.

At the end of testing, after 20,000-wheel passes, the pavement section was trenched to determine the change in thickness of the HMA, base and subgrade layers. Measurements of the HMA layer thickness under the wheel path and away from the wheel path showed no significant difference, indicating that changes to the HMA layer thickness under the wheel path were negligible. Similarly, the subgrade layer thickness was measured at various locations from the centre of the wheel path using a steel ruler, revealing no significant changes in thickness before and after testing. Only the base layer

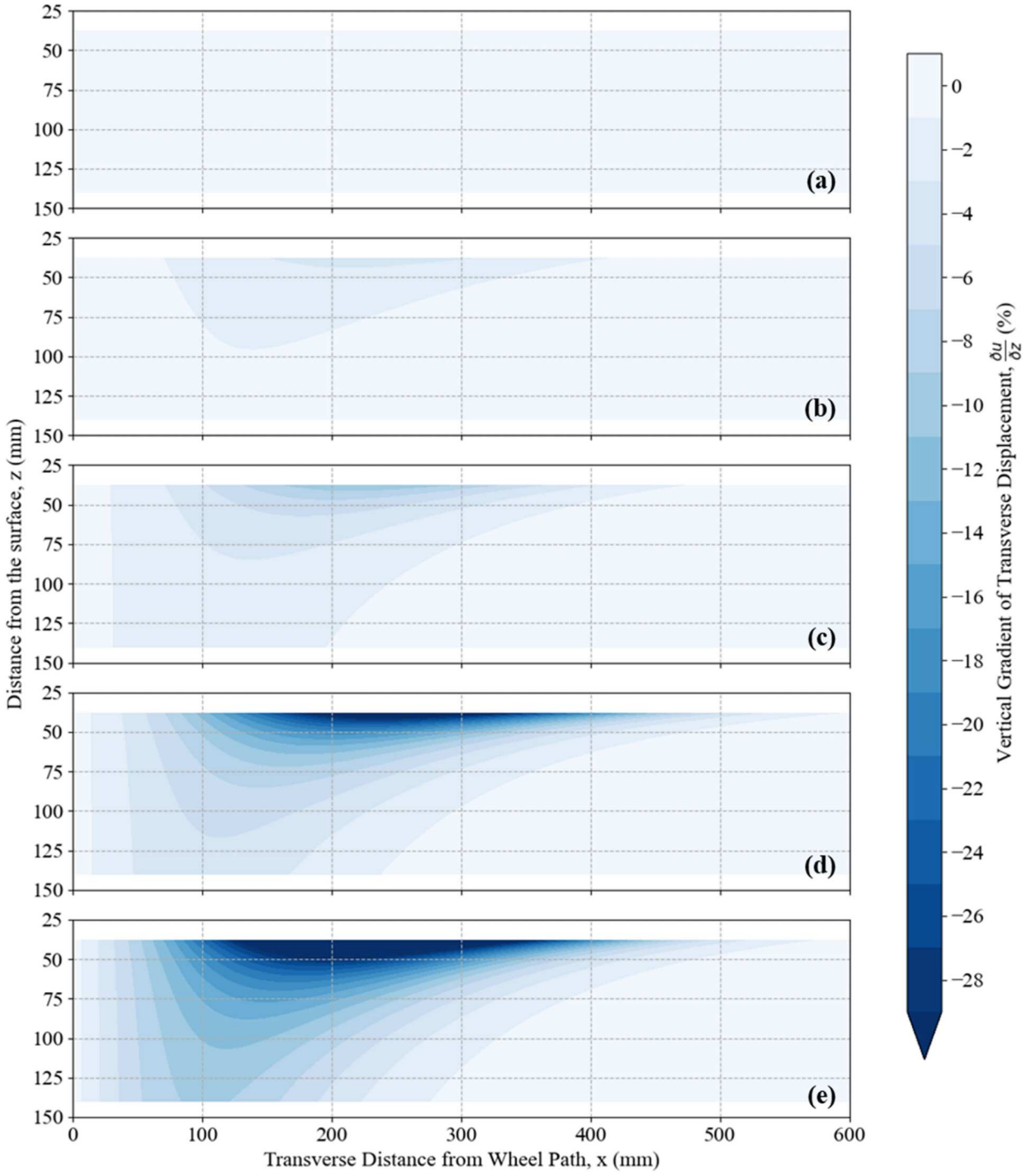

Figure 16. Vertical gradient of transverse displacement (%) after: (a) 100; (b) 1000; (c) 3000; (d) 10,000; and (e) 20,000 passes.

contributed significantly to the overall surface deformation as measured by the surface profilometer. Thus, it can be considered that the deflection profile at the HMA surface equals the change in thickness of the base layer across the pavement section. Using the initial thickness of the base (as constructed) and surface deformation profile (change in base thickness), the average vertical normal strain throughout the thickness of the base can be calculated. Figure 18 compares the average vertical normal strain against the average horizontal normal strain (Figure 17) over the thickness of the base in Figure 18. The x-axis in the figure corresponds to the transverse distance from the centre of the wheel path, while the y-axis corresponds to the average normal strains (%) in the vertical direction (left axis) and horizontal direction (right axis – inverted). Tensile strains are shown as positive normal strains and compressive strains are shown as negative normal strains. The vertical and horizontal normal strains show good agreement, especially at distances greater than 200 mm from the wheel path, i.e. in the compressive zone of horizontal normal strains. In the tensile zone, the horizontal tensile strains were greater in

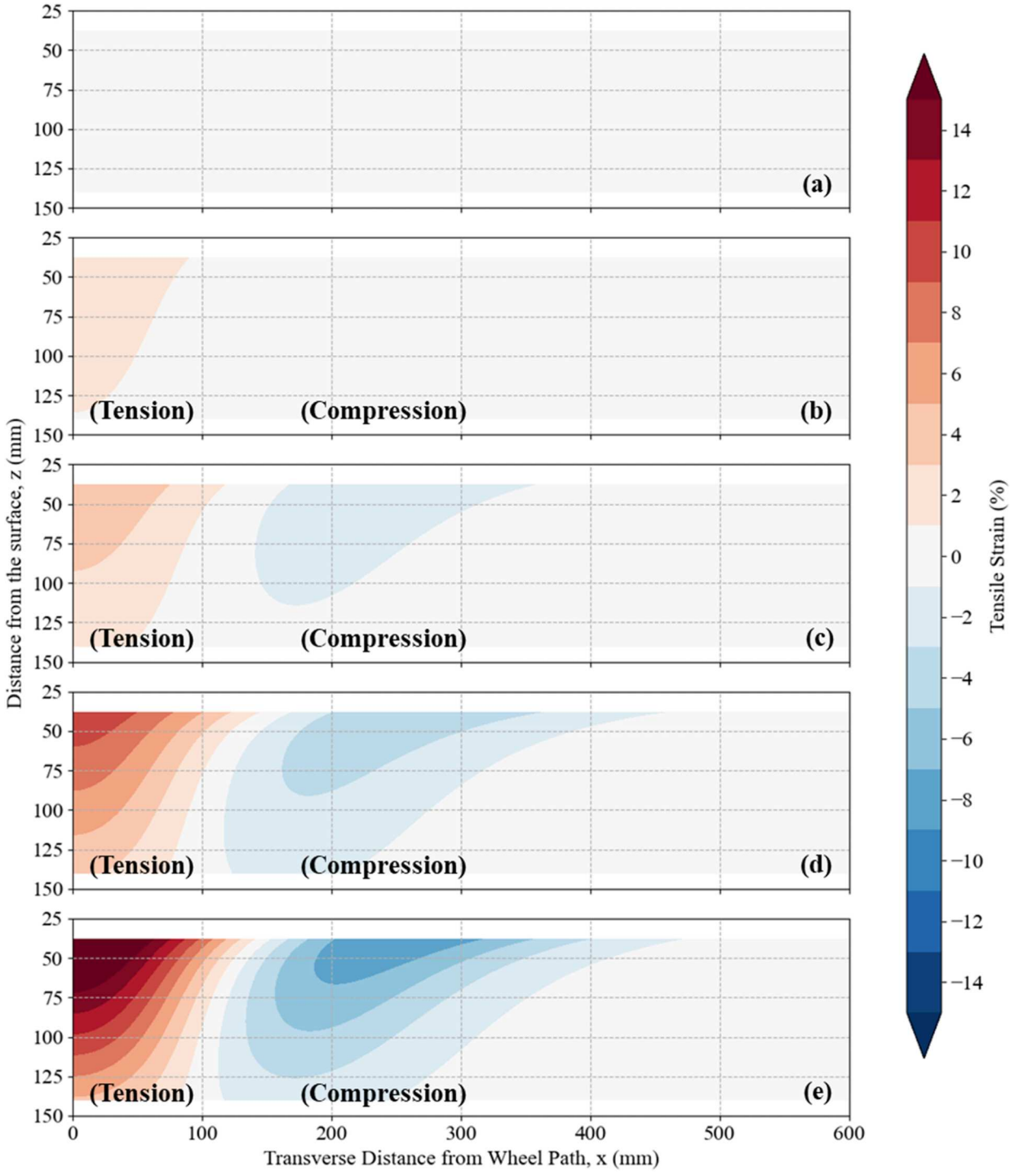

Figure 17. Cumulative horizontal normal strain (%) after: (a) 100; (b) 1000; (c) 3000; (d) 10,000; and (e) 20,000 passes.

magnitude for a given vertical compressive strain, indicating the base is dilatant under those conditions.

Assuming plane strain conditions, the volumetric strains can be calculated as the sum of the vertical and horizontal normal strains. A positive volumetric strain indicates that the base is dilatant since tension is assumed positive for normal strains. Figure 19 shows the average volumetric strain within the base along the distance from the wheel path for increasing number of wheel passes. The base is dilatant in the tensile zone under and in the immediate vicinity of the wheel path, with dilation peaking to a maximum value of 6% between 50 and 75 mm immediately beyond the contact pressure radius (35 mm) at the end of testing (20,000 passes). A peak dilation of 6% is deemed reasonable given that the base was placed at a comparatively high relative density (85%). The base under the wheel path experienced higher confinement levels from the applied wheel load due to the load distribution from the HMA surface layer. This resulted in a lower critical void ratio and, consequently, in a reduced dilation under the wheel path than at locations adjacent to the wheel path that were not subjected to the same level of confinement. In the compressive zones away from the wheel path, although the

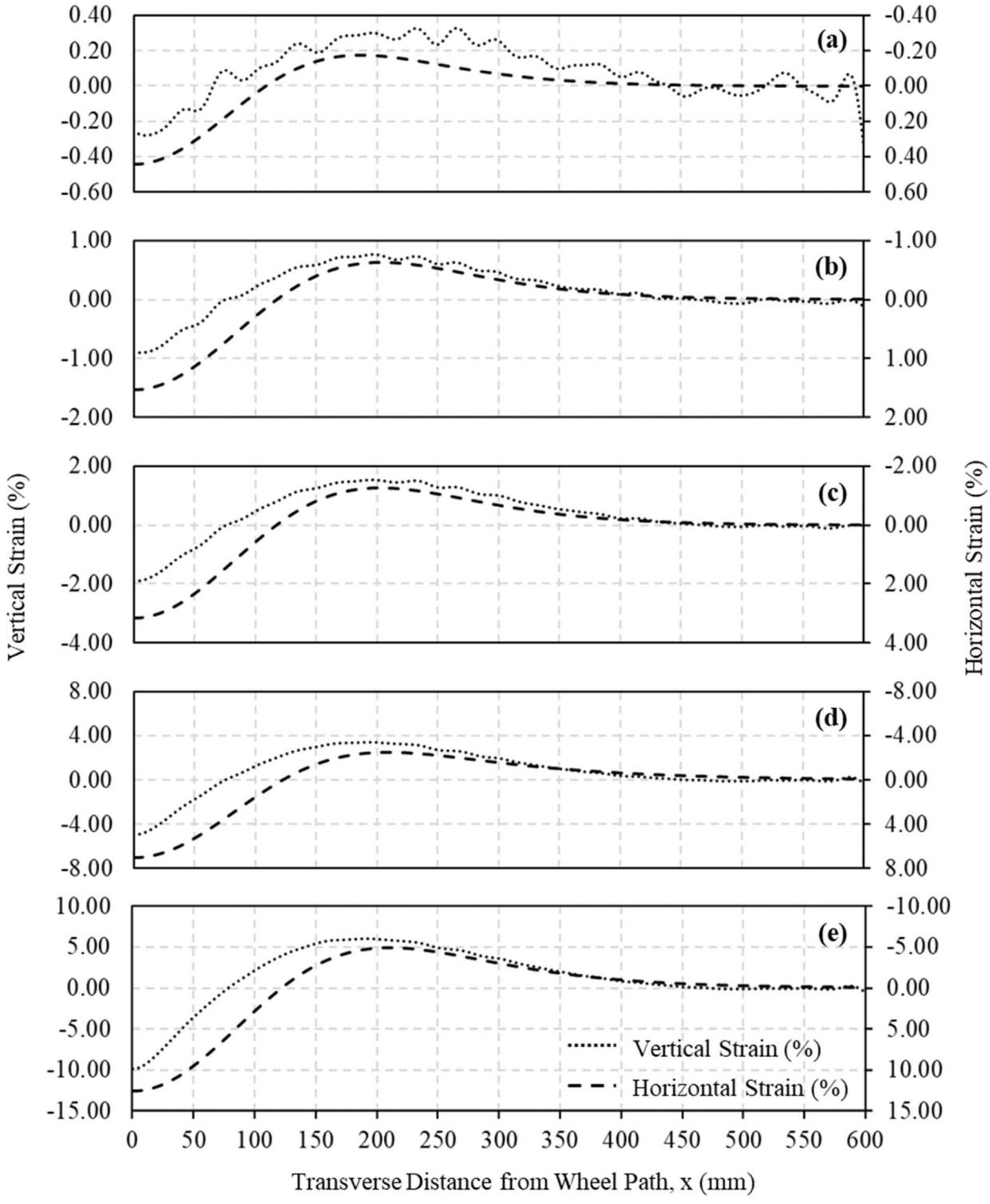

Figure 18. Average vertical vs. horizontal strain after: (a) 100; (b) 1000; (c) 3000; (d) 10,000; and (e) 20,000 passes.

confining pressure due to the load distribution of the HMA layer was lower, the horizontal compressive strains were also lower in magnitude, resulting in negligible dilation.

3.3. Vertical stress distribution

Earth pressure cells installed within the pavement (Figure 3) were used to continuously measure the stress response within the base and subgrade layers under trafficking loads. Figure 20 displays the dynamic stress response of the earth pressure cell located at the base-subgrade interface at the centre of the wheel path. The x-axis shows the time in number of passes (1 pass = 0.5 s) while the y-axis shows the vertical stress as measured by the sensors. The measured stress increased from approximately zero to a maximum value when the wheel load passed over the location of the sensor. The increase in stress under the wheel load for each pass is determined as the vertical stress under trafficking as seen in Figure 20. The vertical stress

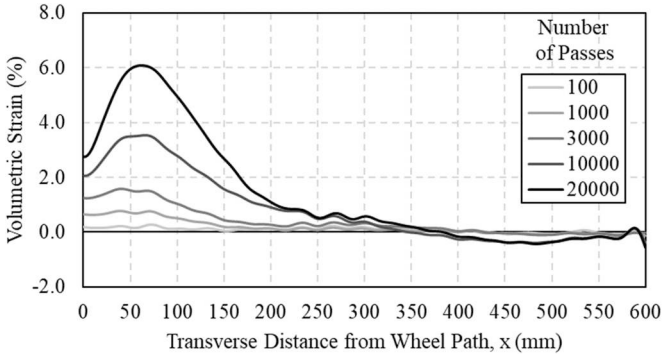

Figure 19. Volumetric strain with increasing number of passes.

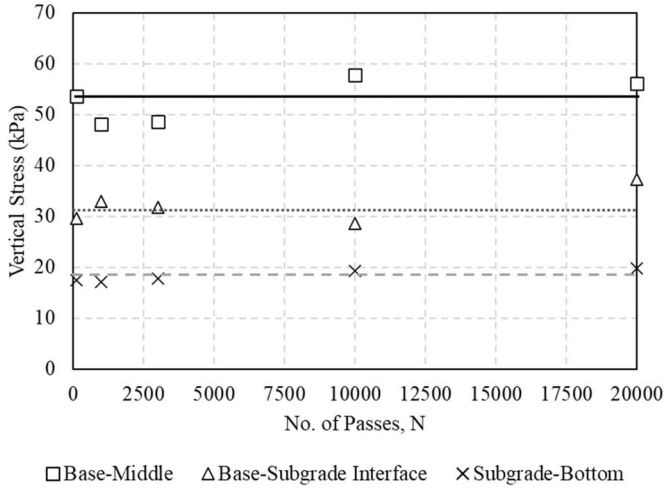

Figure 21. Vertical stress at centre of wheel path with increasing number of passes.

under trafficking at the centre of the wheel path for various depths within the pavement with an increasing number of passes is presented in Figure 21. The vertical stress remained approximately constant, with a slight increase toward the end of the test. The solid, dotted, and dashed lines represent the average vertical stress at the middle of the base, base-subgrade interface, and bottom of the subgrade, respectively, for the duration of testing. The earth pressure cell at the depth closest to the surface (middle of the base) registered the highest vertical stress, while the sensor farthest from the surface recorded the lowest vertical stress, capturing the dissipation of vertical stress with increasing depth within the pavement.

The vertical stress distribution after 10,000-wheel passes at various depths within the pavement is shown in Figure 22. The y-axis shows the vertical stress measured under trafficking at various depths from the surface while the x-axis shows the transverse distance from the sensor locations to the centre of the wheel path (at $x = 0$ mm). While the earth pressure cells were located on either side of the wheel path, a symmetric stress distribution was assumed, showing data points on both sides of the wheel path as measured data. The vertical stress distribution data are fitted with a parameterised form [Equation (7)] of Boussinesq's solution (Nwoji *et al.* 2017) for a vertical stress distribution under a point load.

$$\sigma_{zz} = \frac{3P}{2\pi}\frac{B^3}{\left(\sqrt{x^2 + B^2}\right)^5} \tag{8}$$

where P is the applied wheel load (=2.1 kN); B is the fitting parameter (mm); and x is the transverse distance from the centre of the wheel path (mm).

Fitting using Equation (8) implies that the applied load (P) is consistent with the stress distribution. As previously discussed, the vertical stress under the wheel path decreases with increasing depth. However, this trend is reversed away from the wheel path, with vertical stress increasing with depth at distances of 200 mm from the wheel path, i.e. the stress distribution curves widened at locations deeper within the pavement due to the distribution of the load from the wheel over a larger area. The vertical stress distributions within the base (square markers and solid line in Figure 22) are clearly compatible with the horizontal normal strain distributions previously discussed in Figure 17. The region of horizontal tensile strains ranging from $x = 0$ to 125 mm is roughly the same distance over which the vertical compressive stress went from a maximum of around 60 kPa to less than 5 kPa. While the magnitude of horizontal strains increased with traffic, the compressive and tensile zones in the horizontal normal strain contours remained constant and consistent with the vertical stress distribution, which also remained fairly constant throughout testing.

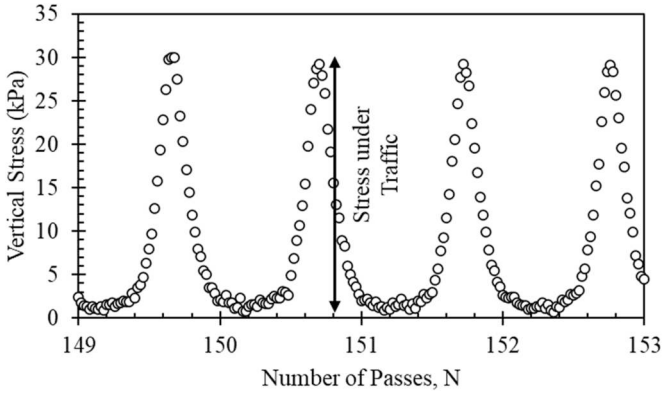

Figure 20. Dynamic response of earth pressure cells under traffic.

4. Conclusions

An accelerated pavement testing facility was developed to assess the performance of reduced-scale pavement sections under controlled environmental conditions in a laboratory setting. The facility allowed quantification of the pavement performance through determination of surface deflections, internal particle movements and stress distributions within the pavement structure. To measure surface deformations under repeated rolling wheel loads, an in-house developed profilometer with a 2D laser distance metre was used to capture surface profiles with increasing trafficking cycles. Post-processing techniques involving the filtering of noise from reflections at sharp particle edges and rough pavement surfaces were developed to process the raw surface profile data into rutting profiles. The profilometer facilitated mapping of the

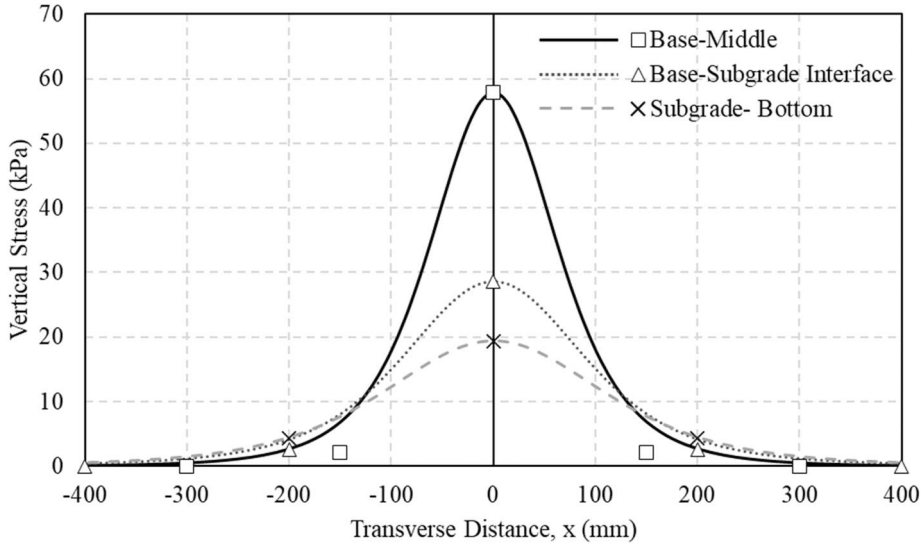

Figure 22. Vertical stress distribution under traffic around 10,000 passes.

pavement surface with a resolution of 1 mm × 1 mm. A unique particle tracking technique was developed to measure subsurface particle movements due to surface deformations. The particle tracking sensors were made of a flexible system of tell-tale wires that offered the least impedance to the response of the pavement layers to external wheel loads. During trafficking, these sensors continuously measured transverse particle displacements perpendicular to the direction of trafficking. A dense array of 30 trackable particles, at a vertical spacing of 25 mm and transverse spacing of 75 mm, was used to measure particle displacements at various depths within the base. The measured data was combined with expected boundary conditions and fitted with a function that closely captured the physical characteristics of the horizontal displacement data. The vertical stress distribution within the pavement under trafficking was measured using earth pressure cells installed at various depths and various transverse distances from the wheel path. The measured surface deformation profiles, subsurface particle displacements and vertical stress distribution within the pavement structure were in agreement and were useful in understanding the mechanism of surface deformation development and the response of the pavement structure to repeated wheel loading.

- The linear progression of the rut with increasing number of wheel passes, and the proportionate increase in heave with the vertical depression under the wheel path indicated that the dominant mechanism of rut development in the test section was lateral flow.
- The top-down progression of the displacement contours with increase in trafficking cycle demonstrated the lateral flow of base aggregates. This was confirmed from the shear transfer efficiency contours obtained from the partial derivative of the displacement contours with respect to the 'z'-axis, which showed a reduction in shear transfer efficiency near the HMA-base interface with increasing number of wheel passes.
- The horizontal normal strain contours, obtained as the partial derivative of the displacement field in the transverse direction, showed a region of tensile strain under the wheel path due to vertical deformations, and regions of compressive strain on either side of the region of tensile strains. It is found that during lateral flow the regions of tension and compression remained more or less a constant with increasing wheel passes, with only the magnitude of the strains increasing.
- The average of the horizontal normal strains, over the thickness of the base, was found to be compatible with the average vertical strain due to surface deformations. The maximum volumetric dilation of the base was estimated at 6% at the end of testing indicating a predominantly steady-state condition within the base layer during rut development.
- The stress distribution within the base layer decreased from its maximum under the wheel path to near zero at about 125 mm from the centre of the wheel path. This was roughly the same distance over which the horizontal normal strain changed from tension to compression indicating compatibility between the stress and strain distributions.

Disclosure statement

No potential conflict of interest was reported by the author(s).

Notes on contributors

S. Subramanian is a Ph.D. in Civil Engineering from the University of Texas at Austin, USA. He specializes in the area of geosynthetic-stabilized aggregate base for flexible pavements. He earned his B. Tech. from the National Institute of Technology, Tiruchirappalli (India), and his M.E. from the Indian Institute of Science, Bengaluru (India)

Jorge G. Zornberg is the Brunswick-Abernathy Regents Professor at the University of Texas at Austin. He has over 35 years' experience in research and practice in geotechnical, geosynthetics, transportation, and geoenvironmental engineering. He earned his B.S. (Hons.) from the National U. of Cordoba (Argentina), his M.S. from PUC-Rio (Rio de Janeiro, Brazil), and his Ph.D. from the U. of California at Berkeley.

ORCID

S. Subramanian http://orcid.org/0000-0001-5151-670X

References

Bhattacharjee, S., and Mallick, R.B., 2012. Effect of temperature on fatigue performance of hot mix asphalt tested under model mobile load simulator. *International Journal of Pavement Engineering*, 13 (2), 166–180.

Epps, A.L., *et al.*, 2001. *Performance prediction with the MMLS3 at Westrack*. College Station, TX: Texas Transportation Institute, Research Report No. FHWA/TX-01/2134-1.

Gehrig, R., *et al.*, 2010. Mobile load simulators – a tool to distinguish between the emissions due to abrasion and resuspension of PM10 from road surfaces. *Atmospheric Environment*, 44 (38), 4937–4943.

Kermani, B., *et al.*, 2018. Experimental simulation and quantification of migration of subgrade soil into subbase under rigid pavement using model mobile load simulator. *Journal of Transportation Engineering, Part B: Pavements*, 144 (4), 04018049.

Kim, H., *et al.*, 2009. Fatigue evaluation of carbon FRP-reinforced porous asphalt composite system using a model mobile load simulator. *Transportation Research Record: Journal of the Transportation Research Board*, 2116, 108–117.

Kim, S.-M., Hugo, F., and Roesset, J.M., 1998. Small-scale accelerated pavement testing. *J. Transp. Eng. ASCE*, 124, 6.

Lee, S.J., and Kim, Y.R., 2004. Development of fatigue cracking test protocol and life prediction methodology using the third scale model mobile loading simulator. *In*: C. Petit, I.L. Al-Qadi et A. Millien, eds. *5th international RILEM conference on cracking in pavements-mitigation, risk assessment and prevention*, 29–36.

Lee, J., Kim, Y.R., and Lee, J., 2015. Rutting performance evaluation of asphalt mix with different types of geosynthetics using MMLS3. *International Journal of Pavement Engineering*, 16 (10), 894–905.

Lee, J., Kim, Y.R., and McGraw, E.O., 2006. Performance evaluation of bituminous surface treatment using third-scale model mobile loading simulator. *Transportation Research Record*, 1958 (1), 59–70.

Lee, S.J., Seo, Y., and Kim, Y.R., 2006. Validation of material-level performance models: using the third-scale model mobile loading simulator. *Transportation Research Record*, 1949 (1), 74–82.

Liu, S., Huang, H., and Qiu, T., 2015, March. Laboratory development and testing of "SMARTROCK" for railroad ballast using discrete element modeling. *In*: *ASME/IEEE joint rail conference*, vol. 56451, p. V001T01A019. American Society of Mechanical Engineers.

Martin, A.E., *et al.*, 2003. Pavement response and rutting for full-scale and scaled APT. *Journal of Transportation Engineering*, 129 (4), 451–461.

National Cooperative Highway Research Program (NCHRP), 2004. *Guide for mechanistic-empirical design of new and rehabilitated pavement structures*. Washington, DC: Transportation Research Board, National Research Council, NCHRP Report 01-37A.

Nwoji, C.U., *et al.*, 2017. Solution of elastic half space problem using Boussinesq displacement potential functions. *Asian Journal of Applied Sciences*, 5 (5), 1087–1093.

Smit, A., *et al.*, 1999. *Report on the first Jacksboro MMLS tests*. Austin, TX: Center for Transportation Research, University of Texas, Research Report No. FHWA/TX-00/0-1814-2.

Smit, A., *et al.*, 2003. Model mobile load simulator testing at National Center for Asphalt Technology test track. *Transportation Research Record*, 1832 (1), 182–190.

Sun, X., and Han, J., 2019. Mechanistic-empirical analysis of geogrid-stabilized layered systems: part I. Solutions. *Geosynthetics International*, 26 (3), 273–285.

Tang, X., Chehab, G.R., and Palomino, A., 2008. Evaluation of geogrids for stabilising weak pavement subgrade. *International Journal of Pavement Engineering*, 9 (6), 413–429. doi:10.1080/10298430802279827.

Tang, X., Stoffels, S., and Palomino, A.M., 2014. Mechanistic-empirical performance prediction of geogrid-modified soft soil subgrade. *In*: *Geo-congress 2014: geo-characterization and modeling for sustainability*, 23–26 February 2014 Atlanta, Georgia, 3054–3061. doi:10.1061/9780784413272.297.

TxDOT SS3239, 2004. *Special specification for thin overlay mix (TOM)*.

van de Ven, M., and Smit, A. de F., 2000. The role of the MMLS devices in APT. *In*: *South African transport conference*, Presented at the Action in Transport for the New Millennium, 16.

Walubita, L.F., 2000. *Accelerated testing of an asphalt pavement with the third-scale model mobile load simulator (MMLS3)*. Thesis (PhD). Stellenbosch University.

Walubita, L.F., Hugo, F., Epps, A.L., 2000. *Performance of rehabilitated lightweight aggregate asphalt concrete pavements under wet and heated model mobile load simulator trafficking: a comparative study with the TxMLS*. Austin, TX: Center for Transportation Research, University of Texas, No. FHWA/TX-00/0-1814-3.

Zornberg, J.G., *et al.*, 1995. Case history: Constructing a geotextile-reinforced slope. *Geotechnical Fabrics Report*, 13 (7), 26–28.